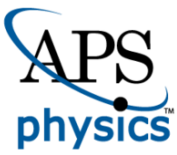

Mechanical Quantum Hall Effect in Time-Modulated Elastic Materials

H. Chen, L.Y. Yao, H. Nassar, and G.L. Huang

Phys. Rev. Applied **11**, 044029 — Published 10 April 2019

DOI: 10.1103/PhysRevApplied.11.044029

Mechanical Quantum Hall Effect in Time-Modulated Elastic Materials

H. Chen[1], L. Y. Yao[2], H. Nassar[1] and G. L. Huang[1*]

[1]Department of Mechanical and Aerospace Engineering, University of Missouri, Columbia, MO 65211, USA

[2]College of Engineering and Technology, Southwest University, Chongqing 400715, China

ABSTRACT

Floquet topological insulators have inspired analogues in photonics, optics, and acoustics, in which non-reciprocal wave propagation in time-modulated materials is achieved due to the breaking of time-reversal symmetry. This paper investigates a mechanical wave analogue of Thouless pumping and the quantum Hall effect (QHE) in one- and two-dimensional periodically time-modulated materials, respectively. In 1D, wave propagation in the time-modulated system is characterized based on the adiabatic theorem, and topologically protected one-way edge modes are numerically demonstrated by the principle of bulk-edge correspondence. In 2D, a time-modulation scheme of a hexagonal lattice is suggested, and polarized edge states characteristics of QHE are put into evidence by the plane wave expansion (PWE) method. The transition from the trivial state to the topological one is captured and interpreted by an invariant Chern number. We numerically demonstrate the existence of topologically protected one-way edge states immune to scattering by sharp corners, defects, randomly disordered modulation phases, and dissipation effects.

Keywords: Quantum Hall effect, Elastic edge waves, Time-modulation, Robust one-way transition.

* Electronic mail: huangg@missouri.edu

1. Introduction

Topological condensed matter systems feature robust unidirectional bandgap-crossing edge states, offering unusual conduction properties [1]. These edge states exhibit immunity to a broad range of structural imperfections, inherently avoiding backscattering over broad energy ranges and circumventing localization in the presence of disorder. Recently, based on an analogy between the Hamiltonian of an electron in a crystal and the dynamical/stiffness matrix of a mechanical lattice, the concept of mechanical topological insulators has emerged [2]. Like their electronic predecessors [3,4], they exhibit an insulating bulk and conducting polarized edge states immune to back-scattering by defects and corners. Edges of topological insulators thus constitute a novel class of superior wave guides with exceptionally robust transmission that can be applied to advanced vibration isolation, signal processing, phononic logic, energy-trapping and harvesting devices [5-9].

Phases of topological insulators are classified based on a quantized invariant, namely the Chern number, attached to a bulk bandgap. As long as the gap remains open, perturbing the constitutive and geometric parameters will have no influence on the qualities of the insulator, which will therefore remain in the same phase with the same Chern number. Conversely, changing the phase of an insulator requires closing the gap. Accordingly, lattices exhibiting Dirac cones, where two bands touch along a single point, are in a critical state; small perturbations that lift the degeneracy can toggle the lattice between a trivial phase with a zero Chern number and a topological phase with a nonzero Chern number. In general, three classes of topological phases have been suggested and observed in acoustic and mechanical systems. For the class of quantum spin Hall insulators (QSHI), the critical state exhibits, in fact, a double Dirac cone with a quadruple degeneracy and shares the same principle of spin-orbit interaction

with quantum spin Hall effect (QSHE) whose topological index is Z_2 invariant [10]. This category of topological phase can be realized by using only passive elements, however, the topological design is critical because spin is not an intrinsic degree of freedom (DOF). Other topological phases such as the quantum valley Hall insulators (QVHI) are based on breaking or keeping other spatial symmetries such as inversion, C_3 or C_6 symmetry [11-18]. Like the QSHE, the QVHI can also be implemented in passive materials; however, it is less robust due to the presence of inter-valley scattering [19]. It is noteworthy that both QSHI and QVHI inducing perturbations must preserve time-reversal symmetry. In contrast, quantum Hall insulators (QHI) necessitate active perturbations that break time-reversal symmetry and thus include non-time-invariant active components [20]. It should be mentioned that only the QHI, which breaks time-reversal symmetry, can guarantee the absence of reflected modes regardless of the nature of the defect. In mechanical systems, topological insulators with strong topological proportion against defects and disorders have indeed been obtained in time-asymmetric gyroscopic systems [21,22]. In fluid acoustics, similar properties can be obtained in networks of acoustic cavities filled with a fluid in motion [23,24]. However, implementing gyroscopic motion in a mechanical lattice is challenging, and the inherent losses and noise in acoustic moving media may become detrimental in most application scenarios.

To address this challenge, an acoustic lattice whose properties are modulated in space and time in a time-harmonic rotating manner, was recently proposed to demonstrate the acoustic analogue of Floquet topological insulators [25]. It has been demonstrated that the acoustic properties of materials can be modulated in a strong manner to open the possibility to broadband, topologically protected, one-way acoustic devices. At the same time, considerable efforts have also been dedicated to mechanical topological insulators for the implementation of unidirectional

transport in 1D time-modulated systems [26,27] and frequency-modulated systems [28]. However, the mechanical analogue of Floquet topological insulators in 2D time-modulated systems has never been investigated and the theoretical modeling and understanding of the system remain highly needed. In practice, a time-modulation of stiffness can be induced by means of programmable piezoelectric components [29-31], trains of shock waves in soft materials [32], magnetorheological elastomers [33], and the photo-elastic effect [34,35]. Recently, an experimental demonstration was reported when unidirectional wave responses at isolated frequencies were observed in a discrete system made of permanent magnets coupled to grounded electromagnets [36].

Here we develop and apply a rigorous full-wave treatment to demonstrate the realistic possibility of mechanical Floquet topological insulators by using time-modulated materials and its application to new concepts for mechanical wave control. First, we study wave propagation in a 1D periodically modulated spring-mass lattice to achieve one-way topologically protected edge modes by using the adiabatic theorem. Topologically protected one-way edge modes are numerically demonstrated by the principle of bulk-edge correspondence. The time evolution of edge modes are quantified using a topological invariant Chern number. The results of the 1D case are then extended to 2D modulated hexagonal lattices. Given the breakage of the time-reversal symmetry, the existence of one-way topologically protected edge states are demonstrated. Lastly, the robustness of one-way topological edge modes and their immunity to backscattering by sharp corners, defects, modulation disorders and dissipation effects are quantitatively analyzed and assessed.

2. Wave propagation in 1D modulated materials

The 1D modulated material is first represented by a 1D 3-periodic spring-mass lattice with a time-dependent modulation on the spring, as shown in Fig. 1(a). The springs are modulated by *T*-periodic functions of time, and constant masses are assumed for simplicity. Note that we adopt the same modulated system as our previous work [26]. Indeed, the main purpose of Ref. 26 is to characterize and quantify the modulation-induced tilt of dispersion bands. However, the main purpose of this study is to show that one-way edge modes exist in the space-frequency (n, ω) plane in 1D modulated media and the time evolution of edge modes can be captured by the Chern number. For theoretical completeness and better readership, we keep a part of Ref. 26 in this section.

2.1 Topological characterization of wave dispersion in 1D media

In general, the titling of wave dispersion bands in the time-periodic system can be captured by using the plane wave expansion (PWE) method [37]. For simplicity, the slow modulation is assumed, therefore, the adiabatic theorem will be applied for analytical modeling of wave propagation in the 1D time-dependent system. As a result, the titled wave dispersion bands can be described by topological invariants: Chern numbers [26]. The three spring constants k_j are modulated in the form of sine waves

$$k_j \equiv k_j(t) = k + \delta k \cos(\nu t + \phi_j), \;\; j = 1, 2, \text{ and } 3, \tag{1}$$

where $\nu = 2\pi / T$ is the modulation frequency, T is its period and ϕ_j is a phase delay. The governing motion equations of the supercell then can be expressed as

$$
\begin{aligned}
m\ddot{u}_1^n(t) &= -(k_3(t)+k_1(t))u_1^n(t) + k_3(t)u_3^{n-1}(t) + k_1(t)u_2^n(t), \\
m\ddot{u}_2^n(t) &= -(k_1(t)+k_2(t))u_2^n(t) + k_1(t)u_1^n(t) + k_2(t)u_3^n(t), \\
m\ddot{u}_3^n(t) &= -(k_2(t)+k_3(t))u_3^n(t) + k_2(t)u_2^n(t) + k_3(t)u_1^{n+1}(t),
\end{aligned} \tag{2}
$$

where $u_j^n \equiv u_j^n(t)$ is the displacement of mass number (j = 1, 2, and 3) of the nth unit cell at time t and a superimposed dot denotes a time derivative.

Based on the adiabatic theorem, the system originally in some eigenstates will remain in that state at later times. Letting ω_m^2 and $\mathbf{\Psi}_m$ be the "instantaneous" eigenvalue and eigenstate, defined by

$$
-\omega_m^2 \mathbf{M}\mathbf{\Psi}_m = -\mathbf{K}(t)\mathbf{\Psi}_m,\ \mathbf{M} = m\mathbf{I}, \mathbf{K}(t) = \begin{bmatrix} k_3+k_1 & -k_1 & -k_3Q^* \\ -k_1 & k_1+k_2 & -k_2 \\ -k_3Q & -k_2 & k_2+k_3 \end{bmatrix}, \tag{3}
$$

where $\mathbf{I}$ is the 3×3 identity matrix, q is dimensionless wavenumber, Q^* is the conjugate of Q as $Q^* = e^{-iq}$, and the time-periodic stiffness matrix satisfies $\mathbf{K}(t+T) = \mathbf{K}(t)$. Note that the eigenstates are normalized to satisfy $\langle \mathbf{\Psi}_m, \mathbf{M}, \mathbf{\Psi}_n \rangle = \delta_{mn}$, with δ_{mn} being the Kronecker symbol and the brackets denoting the underlying Hermitian inner product. Then, for a given q, the displacement field of the system can be determined from the nth snapshot Floquet-Bloch eigenmode as [26]

$$
\mathbf{\Phi}_n(t) = \frac{\mathbf{\Psi}_n(t)}{\sqrt{\omega_n(t)/\omega_n(0)}} \exp\left[i\int_0^t \left(\omega_n(s) + \dot{\gamma}_n(s)\right) \mathrm{d}s \right], \tag{4}
$$

with

$$
\dot{\gamma}_n = \mathrm{Im}\left\langle \mathbf{\Psi}_n, \mathbf{M}, \dot{\mathbf{\Psi}}_n \right\rangle, \tag{5}
$$

provided that ω_n^2 remains a nondegenerate eigenvalue at all instants in time. In particular, if the nth band is separated by gaps from bands ($n \pm 1$)th at $t = 0$, then it will remain so at all subsequent time. If not, scattering from one band to another will occur and will invalidate the theorem. It should be mentioned that the nondegenerate eigenmodes can be deemed as robust and topologically protected.

To quantify the change of the wave dispersion bands due to the slow modulation, the Chern number of each band will be characterized by

$$C_n = \frac{1}{2\pi}\int_{-\pi}^{\pi}\int_0^T B_n \mathrm{d}q\mathrm{d}t, \tag{6}$$

where the Berry curvature is defined as $B_n = \nabla \times \mathbf{A}_n$, with $\mathbf{A}_n = (A_n^t, A_n^q) = \left(\mathrm{Im}\left\langle \mathbf{\Psi}_n, \mathbf{M}, \dot{\mathbf{\Psi}}_n \right\rangle, \mathrm{Im}\left\langle \mathbf{\Psi}_n, \mathbf{M}, \partial_q \mathbf{\Psi}_n \right\rangle\right)$ forming a vector called Berry connection.

Figure 2 shows the evolution of dispersion curves of a 3-periodic modulated lattice as a function of the non-dimensional wavenumber and time. The parameters used are $m = 1$, $k = 1$, $\delta k = 0.2k$, $v = 0.005$, $\phi_1 = 0$, $\phi_2 = 2\pi/3$, and $\phi_3 = 4\pi/3$. Because the dispersion bands are spectrally separated, the individual bands can be quantified by the Chern numbers based on Eq. (6), which is $C_1 = -1$, $C_2 = 2$, and $C_3 = -1$, respectively, for the first, second and third dispersion bands. It is noticed that when the crystal has a finite number of bands, the sum of the Chern numbers over all bands is zero, implying the remarkable result that the sum of all dispersion tilts vanishes. To demonstrate robustness of the Chern number, Fig. 3(a) shows the phase diagram of the Chern number in function of phase delays $\{\phi_1, \phi_2, \phi_3\}$ interpreted as barycentric coordinates in the planes $(\phi_1 + \phi_2 + \phi_3 = 2\pi, m_1 = m_2 = m_3 = m)$. It is found that only two arrays of the Chern numbers,

namely ±(1,−2,1) are obtained with different relative values of the phase delays ϕ_j, j = 1, 2, and 3, under topological protection of constant masses m. It should be emphasized that when only masses are modulated, as our previous work [26], Chern numbers of the system is zero, which means there is no edge mode by using the corresponding parameters. Figure 3 also reveals that if constant across large regions, the Chern number is insensitive to uncertainty in the phase delays and in the values of the masses except near critical lines where phase transitions occur. This could also generalize to other forms of uncertainty. For instance, changing the sinusoidal modulation into a triangular one while leaving the other parameters unchanged, perturbs the dispersion diagram but ultimately has zero influence on the Chern numbers [26].

2.2 Bulk-edge correspondence

According to the principle of bulk-edge correspondence [38,39], a nonzero Chern number supports the existence of topological edge states. Here, numerical simulations will be performed to calculate dispersion relations of a finite time-modulated lattice and the corresponding edge states to confirm the bulk-edge correspondence. The evolution of the frequency spectrum of a finite modulated lattice over one-period of modulation is shown in Fig. 4. In the simulation, the lattice is composed of 300 masses and under free boundary conditions. The modulation parameters are $\delta k = 0.2k$, $\phi_1 = 0$, $\phi_2 = 2\pi/3$, $\phi_3 = 4\pi/3$, and the modulation frequency is v = 0.005, such that the eigenmodes of the lattice can be calculated directly from the dynamic matrix $\mathbf{M}^{-1}\mathbf{K}$ at any time instant. It can also be observed in Fig. 4 that a pair of edge states are populated within two bulk bandgaps. This confirms the prediction that a modulated media can host two-edge states at the boundaries in a time periodical fashion by breaking time-reversal symmetry. To confirm the bulk-edge correspondence, Fig. 5 shows a zoomed view of the time evolution of eigenfrequencies inside the higher bandgap and the corresponding eigenmodes as a

function of position along the lattice. To illustrate the time evolution of the edge-bulk states, the left edge state (state b) denoted in Fig. 5(b) is selected as a starting point. Its mode is marked by blue circles in Fig. 5(a). This state remains when the frequency is decreased (state c) as long as its frequency is within the gap. When the frequency is decreased further in the passing band, the left edge state changes to a bulk state. Notably, once the mode returns into the gap, it appears localized at the opposite boundary (state e). As the frequency increases, state e transforms into state f then bulk state g which, by a similar mechanism, transforms back into state b, and so on. This implies that the system changes its wave characteristics with time, as we see edge modes appearing, interchanging, and then disappearing. Note however that the cycle b-c-d-e-f-g does not represent the transient propagation of a physical signal; only b-c and e-f do. As a matter of fact, b-c and e-f transitions are adiabatic, meaning that snapshot states are identical to transient states by the adiabatic theorem [26]. On the other hand, transitions c-e and b-f are not adiabatic since, according to Fig. 5(a), the gaps separating states c and f from the passing bands become vanishingly small, at which time these states will be scattered into bulk modes. In that case, snapshot states and transient states will differ significantly. To quantify the time evolution of the state change, we provide the numerical observation of Chern numbers for the dispersion relations in the time-modulated infinite lattice. Specifically, the gap Chern number C_{gap}, which is the summation of the Chern numbers below the bandgap will be used as topological characteristics of edge states [40]. A bandgap with $C_{\text{gap}} = 0$ is trivial, while a bandgap with $C_{\text{gap}} \neq 0$ is topologically nontrivial. For the lattice with the modulation scheme $\{\phi_1, \phi_2, \phi_3\} = \{0, 2\pi/3, 4\pi/3\}$, the Chern numbers of the bands are $C = \{-1, 2, -1\}$, respectively. In this case, there is a unique edge state: $C_{\text{gap}} = C_1 + C_2 = 1,$ for the higher bandgap as shown in Fig. 5. Similarly, the number

of edge states in the lower bandgap is also equal to one based on the gap Chern number $C_{\text{gap}} = C_1 = -1$. The sign of the gap Chern numbers indicates the different edge wave direction.

To further support the above observation, the transient response of the finite lattice with modulated spring constants is numerically simulated using the finite difference method. The horizontal loading force is an 80-cycle narrow-band tone burst imposed at the left edge of the lattice, as shown in Fig. 6(a). The applied force is given as

$$F = A_0[H(t-0.4T) - H(t-0.4T-N/f_c)][1-\cos(\omega_c(t-0.4T)/N)]\sin(\omega_c(t-0.4T), \qquad (7)$$

where A_0 is the amplitude, $f_c = \omega_c/2\pi$ is the central frequency, H is the Heaviside function and N is the number of cycles. The parameters used are $A_0 = 100$, and $\omega_c = 1.75$. The displacement field at different times are Fourier-analyzed in the time domain to obtain $U_{n,\omega}$ whose amplitude is plotted as level sets over the (n, ω) plane in Figs. 6(b)-(d). In the (n, ω)-space, the evolution corresponds to a one-way edge state moving anticlockwise. Therein, the left and right boundaries correspond to the free boundaries of the sample, whereas the top and bottom boundaries correspond to the boundaries of the higher bulk bandgap. It should be noted that if we flip the sign of the modulation frequency, the above observations would be reversed. Thus, this time-dependent bulk-edge correspondence indicates breaking for time-reversal symmetry.

2.3 Robustness analysis

In this section, we discuss the robustness of the topologically protected edge mode against modulation phase disorders and dissipation effects. For disorder in phase delay, we allow ϕ_j, j = 1, 2, and 3 to be randomly displaced $\delta\phi_j$ with respect to its original phase delays $\{\phi_1, \phi_2, \phi_3\} = \{0, 2\pi/3, 4\pi/3\}$, as shown by the purple circles in Figs. 7(a) and (c). The phase disorder degree is defined as 100% $\max\left(\left|\delta\phi_j\right|\right)\Big/\left(2\pi/3\right)$. Figures 7(b) and (d) show the evolution

of the frequency spectra of a finite modulated lattice for two different disorder degrees: 20% and 40%. In the simulation, we keep rest of parameters the same. We can clearly see that the resulting edge modes are always inside the bandgap and does not coalesce with the bulk bands even under the strong disorder perturbation. We then evaluate the dissipation effects on edge modes and consider the dissipation induced force $f_j = \eta v_j$ ($j = 1, 2, 3$), where η and v_j are the damping coefficient of springs and the velocity of the jth mass, as shown in Fig. 8. In Figs. 8(a) and (c), it is clearly evident that the damping strength η from $10^{-10}k$ to $10^{-6}k$ cannot affect the real parts of the eigenvalues. The dissipation induced damping, which corresponds to the imaginary parts of the eigenvalues, is shown in Figs. 8(b) and (d). It can be seen that all eigenstates are damped, but the damping rate is much smaller than the real part. Hence, the topologically protected edge mode in this 1D modulated material is robust against the phase disorder and damping perturbations.

3. Wave propagation in 2D modulated hexagonal materials

In this section, a mechanical analogue of the QHI is implemented into a 2D modulated material. To be general, the assumption of the slow modulation is taken out. In this 2D protocol, we employ the high-frequency modulation. As such, the high-frequency expansion can be used as an alternative method, which can generate a static effective Hamiltonian and it is easier to treat than the original Floquet Hamiltonian [41,42]. However, compared with the high-frequency expansion method, the PWE method has advantages in formulating and can be applied for the cases with large modulation amplitude. In addition, the phase transitions from nontrivial to trivial states can be captured with the PWE method. Therefore, the PWE method will be used for studying wave propagation in the 2D modulated medium.

3.1 Governing equations

The 2D modulated elastic medium is represented by a modulated hexagonal lattice shown in Fig. 9, which is periodic invariant by translation along the lattice vectors $\mathbf{r}_1$, $\mathbf{r}_2$, $\mathbf{r}_3$ and any integer combination thereof. The modulated hexagonal lattice is composed of modulated trimers connected together along the hexagonal bonds via constant springs denoted by *J*. The modulated trimer is formed by three masses interconnected with modulated springs as $k_j = k + \delta k \cos(\nu t + \phi_j)$, for j = 1, 2, and 3. Thus, the unit cell of the lattice contains six masses of equal value, *m*, and a total of twelve degrees of freedom and nine springs. Letting $\mathbf{u}_g$ be the displacement vectors of mass *g* (*g* = 1-6) interior to the unit cell, and $\mathbf{q}$ be a wavenumber, all other displacements of the boundary nodes can be deduced through

$$\mathbf{u}_7 = Q_1\mathbf{u}_6, \qquad \mathbf{u}_8 = Q_2\mathbf{u}_4, \qquad \mathbf{u}_9 = Q_3\mathbf{u}_5, \tag{8}$$

where Q_j is the phase factor $e^{i\langle \mathbf{q},\mathbf{r}_j\rangle}$, for j = 1, 2, and 3. Consequently, the equations of motion within one unit-cell can be expressed as

$$\begin{aligned}
m\ddot{\mathbf{u}}_1 &= k_2\langle \mathbf{u}_3-\mathbf{u}_1,\mathbf{r}_2\rangle\mathbf{r}_2 + k_3\langle \mathbf{u}_2-\mathbf{u}_1,\mathbf{r}_3\rangle\mathbf{r}_3 + J\langle \mathbf{u}_4-\mathbf{u}_1,\mathbf{r}_1'\rangle\mathbf{r}_1',\\
m\ddot{\mathbf{u}}_2 &= k_3\langle \mathbf{u}_1-\mathbf{u}_2,\mathbf{r}_3\rangle\mathbf{r}_3 + k_1\langle \mathbf{u}_3-\mathbf{u}_2,\mathbf{r}_1\rangle\mathbf{r}_1 + J\langle \mathbf{u}_5-\mathbf{u}_2,\mathbf{r}_2'\rangle\mathbf{r}_2',\\
m\ddot{\mathbf{u}}_3 &= k_1\langle \mathbf{u}_2-\mathbf{u}_3,\mathbf{r}_1\rangle\mathbf{r}_1 + k_2\langle \mathbf{u}_1-\mathbf{u}_3,\mathbf{r}_2\rangle\mathbf{r}_2 + J\langle \mathbf{u}_6-\mathbf{u}_3,\mathbf{r}_3'\rangle\mathbf{r}_3',\\
m\ddot{\mathbf{u}}_4 &= k_2\langle Q_2^*\mathbf{u}_6-\mathbf{u}_4,\mathbf{r}_2\rangle\mathbf{r}_2 + k_3\langle Q_3\mathbf{u}_5-\mathbf{u}_4,\mathbf{r}_3\rangle\mathbf{r}_3 + J\langle \mathbf{u}_1-\mathbf{u}_4,\mathbf{r}_1'\rangle\mathbf{r}_1',\\
m\ddot{\mathbf{u}}_5 &= k_3\langle Q_3^*\mathbf{u}_4-\mathbf{u}_5,\mathbf{r}_3\rangle\mathbf{r}_3 + k_1\langle Q_1\mathbf{u}_6-\mathbf{u}_5,\mathbf{r}_1\rangle\mathbf{r}_1 + J\langle \mathbf{u}_2-\mathbf{u}_5,\mathbf{r}_2'\rangle\mathbf{r}_2',\\
m\ddot{\mathbf{u}}_6 &= k_1\langle Q_1^*\mathbf{u}_5-\mathbf{u}_6,\mathbf{r}_1\rangle\mathbf{r}_1 + k_2\langle Q_2\mathbf{u}_4-\mathbf{u}_6,\mathbf{r}_2\rangle\mathbf{r}_2 + J\langle \mathbf{u}_3-\mathbf{u}_6,\mathbf{r}_3'\rangle\mathbf{r}_3',
\end{aligned} \tag{9}$$

where Q_j^* is the conjugate of Q_j as $Q_j^* = e^{-i\langle \mathbf{q},\mathbf{r}_j\rangle}$. Recalling that $\langle \mathbf{u}_g,\mathbf{r}_k\rangle\mathbf{r}_k = \mathbf{r}_{kk}\mathbf{u}_g$ with $\mathbf{r}_{kk} = \mathbf{r}_k \otimes \mathbf{r}_k$, the governing equations can be rewritten in compact matrix form as

$$\mathbf{M}\ddot{\mathbf{u}} = -\mathbf{K}\mathbf{u}, \quad \mathbf{M} = m\mathbf{I} \tag{10}$$

with

$$\ddot{\mathbf{u}}=\begin{bmatrix}\mathbf{u}_1\\ \mathbf{u}_2\\ \mathbf{u}_3\\ \mathbf{u}_4\\ \mathbf{u}_5\\ \mathbf{u}_6\end{bmatrix},\quad \mathbf{K}=\begin{bmatrix} k_2r_{22}+k_3r_{33}+Jr_{11}' & -k_3r_{33} & -k_2r_{22} & -Jr_{11}' & 0 & 0\\ -k_3r_{33} & k_3r_{33}+k_1r_{11}+Jr_{22}' & -k_1r_{11} & 0 & -Jr_{22}' & 0\\ -k_2r_{22} & -k_1r_{11} & k_1r_{11}+k_2r_{22}+Jr_{33}' & 0 & 0 & -Jr_{33}'\\ -Jr_{11}' & 0 & 0 & k_2r_{22}+k_3r_{33}+Jr_{11}' & -k_3Q_3r_{33} & -k_2Q_2^*r_{22}\\ 0 & -Jr_{22}' & 0 & -k_3Q_3^*r_{33} & k_3r_{33}+k_1r_{11}+Jr_{22}' & -k_1Q_1r_{11}\\ 0 & 0 & -Jr_{33}' & -k_2Q_2r_{22} & -k_1Q_1^*r_{11} & k_1r_{11}+k_2r_{22}+Jr_{33}' \end{bmatrix}, \tag{11}$$

where $\mathbf{I}$ is the 12×12 identity matrix,

$$\mathbf{r}_1=\begin{bmatrix}1\\0\end{bmatrix},\quad \mathbf{r}_2=\begin{bmatrix}-1/2\\-\sqrt{3}/2\end{bmatrix},\quad \mathbf{r}_3=\begin{bmatrix}-1/2\\\sqrt{3}/2\end{bmatrix}, \tag{12}$$

and

$$\mathbf{r}_1'=\begin{bmatrix}0\\1\end{bmatrix},\quad \mathbf{r}_2'=\begin{bmatrix}\sqrt{3}/2\\-1/2\end{bmatrix},\quad \mathbf{r}_3'=\begin{bmatrix}-\sqrt{3}/2\\-1/2\end{bmatrix}. \tag{13}$$

3.2 Topological characterization of wave dispersion in 2D media

Based on Floquet-Bloch theorem in the time domain, we have

$$\mathbf{u}=\sum_{p=-\infty}^{\infty}\mathbf{a}^p e^{i(\omega+p\nu)t}, \tag{14}$$

where $\mathbf{a}^p$ is the pth vector of displacement amplitudes. The spring constants are periodic functions of time with period $T=2\pi/\nu$ such that $\mathbf{K}(t)=\mathbf{K}(t+T)$. Accordingly, the stiffness matrix can be expanded in terms of their Fourier series and expressed as

$$\mathbf{K}(t)=\sum_{l=-\infty}^{\infty}e^{ilvt}\mathbf{K}^l, \tag{15}$$

where $\mathbf{K}^l$ is the corresponding matrix coefficient. Substituting Eqs. (14) and (15) into Eq. (10) and performing harmonic balance, we obtain the following infinite set of coupled time-independent equations with frequency $\omega+p\nu$

$$\sum_{l=-\infty}^{\infty}K^l\mathbf{a}^{p-l}=(\omega+p\nu)^2\mathbf{M}\mathbf{a}^p. \tag{16}$$

For the case of weak modulation, Eq. (16) can then be truncated to the three harmonics $p = \{-1, 0, 1\}$ to obtain the dispersion diagram of this system so that the following relation holds

$$\omega^2 \mathbf{M}\mathbf{x} + \omega \mathbf{C}\mathbf{x} + \mathbf{D}\mathbf{x} = \mathbf{0} \tag{17}$$

with

$$\mathbf{M} = m\begin{bmatrix} \mathbf{I} & \mathbf{0} & \mathbf{0} \\ \mathbf{0} & \mathbf{I} & \mathbf{0} \\ \mathbf{0} & \mathbf{0} & \mathbf{I} \end{bmatrix}, \mathbf{C} = m\begin{bmatrix} -2\nu\mathbf{I} & \mathbf{0} & \mathbf{0} \\ \mathbf{0} & \mathbf{0} & \mathbf{0} \\ \mathbf{0} & \mathbf{0} & 2\nu\mathbf{I} \end{bmatrix}, \mathbf{D} = \begin{bmatrix} \nu^2 m\mathbf{I} - \mathbf{K}^0 & -\mathbf{K}^{-1} & \mathbf{0} \\ -\mathbf{K}^1 & -\mathbf{K}^0 & -\mathbf{K}^{-1} \\ \mathbf{0} & -\mathbf{K}^1 & \nu^2 m\mathbf{I} - \mathbf{K}^0 \end{bmatrix}, \mathbf{x} = \begin{bmatrix} \mathbf{a}^{-1} \\ \mathbf{a}^0 \\ \mathbf{a}^1 \end{bmatrix}. \tag{18}$$

To solve the quadratic eigenvalue problem in Eq. (17), a transformation method will be adopted by converting it into a linear eigenvalue problem. Letting

$$\mathbf{\Psi} = \begin{bmatrix} \omega\mathbf{x} \\ \mathbf{x} \end{bmatrix}, \tag{19}$$

and preserving the symmetry property, we can rewrite Eq. (17) as

$$\mathbf{R}\mathbf{\Psi} = \omega\mathbf{S}\mathbf{\Psi} \tag{20}$$

with

$$\mathbf{R} = -\begin{bmatrix} \mathbf{C} & \mathbf{D} \\ \mathbf{D} & \mathbf{0} \end{bmatrix}, \quad \mathbf{S} = \begin{bmatrix} \mathbf{M} & \mathbf{0} \\ \mathbf{0} & \mathbf{-D} \end{bmatrix}. \tag{21}$$

From Eq. (20), the associated dispersion diagram can then be obtained from the condition of a zero determinant as

$$\det(\mathbf{R} - \omega\mathbf{S}) = 0. \tag{22}$$

Similar to the 1D case, the Chern number will be numerically calculated to characterize the topological properties and a topological invariant of the bulk bands due to the modulation. The Berry curvature for the nth band of interest can be numerically determined by [26]

$$B_n = \nabla \times \mathbf{A} = \partial_{q_x} A_y - \partial_{q_y} A_x = 2\,\mathrm{Im} \sum_{m \neq n} \frac{\left\langle \mathbf{\Psi}_n, \partial_{q_x}\mathbf{R} - \partial_{q_x}\mathbf{S}, \mathbf{\Psi}_m \right\rangle \left\langle \mathbf{\Psi}_m, \partial_{q_y}\mathbf{R} - \partial_{q_y}\mathbf{S}, \mathbf{\Psi}_n \right\rangle}{\left(\omega_n - \omega_m\right)^2}, \tag{23}$$

where $\mathbf{A} = \mathrm{Im}\left\langle \boldsymbol{\Psi}_n, \mathbf{M}, \partial_{\mathbf{q}} \boldsymbol{\Psi}_n \right\rangle$ is the Berry connection. Note that the eigenvectors are normalized to satisfy

$$\left\langle \boldsymbol{\Psi}_m, \mathbf{S}, \boldsymbol{\Psi}_n \right\rangle = \delta_{mn} \tag{24}$$

with δ_{mn} being the Kronecker symbol. The Berry curvature is then integrated over the entire Brillouin zone to obtain the Chern number of the nth band as

$$C_n = \frac{1}{2\pi} \iint_{\mathrm{BZ}} B_n \mathrm{d}q_x \mathrm{d}q_y. \tag{25}$$

3.3 Topological edge and interface states

In this section, the dispersion diagram of the mechanical lattice with/without time-dependent modulation will be investigated based on the proposed PWE method. Then, the topological characterization of the dispersion bands will be conducted, which will be used for prediction of topological edge and interface states of the modulated elastic media.

Based on Eq. (22), dispersion relations of the non-modulated mechanical 2D lattice in Fig. 9 are obtained and plotted in Fig. 10. Here, the lattice parameters used are m = 1, k = 10, J = 0.5, and v = 12. From Fig. 10, three degenerate points at wavenumber K are found at ω = 0.49, ω = 3.91, and ω = 5.52, respectively, in the non-modulated system. To inspect wave propagation at those degenerate points, two corresponding wave modes at each degenerate point are also plotted in Figs. 10(b)-(d), which are illustrated by the mass trajectories at different times. As shown in Fig. 10(b) for ω = 5.52, one eigenmode has zero displacement at the boundaries of the unit cell and contains three inner masses moving in-phase along a straight orbit. In contrast, another mode has in-phase maximum displacement by a phase delay of $2\pi/3$ at the boundaries of the unit cell and zero displacement for the three inner masses. In Fig. 10(c) for ω = 3.91, one mode describes positively oriented circular orbits of the inner masses within the unit cell and they are delayed by

a phase delay of $2\pi/3$ with respect to each other. In comparison, another mode is represented by negatively oriented circular orbits of the masses along the boundaries of the unit cell with a phase delay of $2\pi/3$. In Fig. 10(d) for $\omega = 0.49$, two modes describe the circular orbits for the six masses within the unit cell. One mode has positively oriented circular in-phase motion with the large displacements for inner masses and negatively oriented circular motion with small displacements of masses at the boundaries of the unit cell by a phase delay of $2\pi/3$ with respect to each other. Another mode switches the state containing the reverse motions and amplitudes for the masses within the unit cell.

By calculating angular momentum bias for those eigenmodes at three degenerate frequencies [20], a strong opposite polarization of two eigenmodes at the frequency $\omega = 3.91$ can be clearly identified, and therefore the degeneracy of the Dirac cone could be lifted by the phase perturbing of the spring constant k to break the temporal symmetry; see Fig. 11(a). To demonstrate the phenomena, dispersion relations of the modulated mechanical 2D lattice is calculated and shown in Figs. 11(b)-(d). In the figure, the spring constant k is modulated in function of $k_j = k + \delta k \cos(\nu t + \phi_j)$, with k = 10 for j = 1, 2, and 3 by applying a clockwise modulation scheme $\{\phi_1, \phi_2, \phi_3\} = \{0, 2\pi/3, 4\pi/3\}$, ν = 12 in the trimers and the modulation amplitudes are $\delta k = 0.1k$, $0.2k$, $0.3k$, respectively. The coupling spring constant is kept as $J = 0.5$. Here we focus on the four bands around the degenerate frequency $\omega = 3.91$, for which a dipolar profile is observed by the time modulation. For convenience of comparison, the dispersion relations of the non-modulated lattice at the four bands around the degenerate frequency ω = 3.91 are also plotted (blue dashed curves, $\delta k = 0$). For the modulated lattice, dispersion curves fold along the frequency axis with periodicity equal to the modulation frequency and degeneracy are lifted both at Γ and K points by an amount proportional to the modulation strength. As δk

increases, the upper and lower parts of the Dirac cones separate further and a larger bandgap opens. It is also of interest to note that bandgap opening is accompanied by band inversion phenomena at point K. It is important to note that modes exchange places as the softer and stiffer springs exchange places, and the frequency magnitude given by the spectral span of the unmodulated (blue dashed) band structure, is smaller than the modulation frequency $v = 12$. This ensures that no mode transitions between different Floquet bands occur, and bands of different origin and different Floquet orders remain separate from each other.

To verify the topology nature of the degeneracy, Berry curvatures of the four topological bands in Fig. 11 for the modulated lattice are calculated and plotted in Fig. 12 based on Eq. (23), from which the corresponding Chern number can also be numerically determined by integrating over the entire Brillouin zone. We found that the four bands of interest possess topological indices $C = \{1, 0, 0, -1\}$ for the clockwise modulation scheme $\{\phi_1, \phi_2, \phi_3\} = \{0, 2\pi/3, 4\pi/3\}$. However, if we reverse the modulation scheme from clockwise to anticlockwise $\{\phi_1, \phi_2, \phi_3\} = \{4\pi/3, 2\pi/3, 0\}$, equivalent to time reversal, the reversal of the Chern numbers $C = \{-1, 0, 0, 1\}$ is expected. The system switches from trivial to nontrivial topology as we turn on the modulation, and the modulated system does not exhibit a topological phase transition. To illustrate the robustness, the phase diagram of Chern numbers for the four bands in a function of phase delays $\{\phi_1, \phi_2, \phi_3\}$ is interpreted as barycentric coordinates in the planes ($\phi_1 + \phi_2 + \phi_3 = 2\pi$); see Fig. 13. It can be found that the Chern numbers for the four bands of interest are constant across large regions and insensitive to uncertainty in the phase delays except near critical lines where phase transitions occur. This robustness could generalize to other forms of uncertainty. For instance, changing the sinusoidal modulation into a triangular one while the other parameters

are left unchanged, perturbs the dispersion diagram but ultimately has no influence on the Chern numbers.

One of the most appealing features of topological insulators is the existence of one-way edge modes at the boundaries between domains of different topology. The number of topological edge states supported by a given interface is also dictated, similar to the bulk-boundary correspondence principle discussed in the 1D case, by the gap Chern numbers of all the bulk bands below the corresponding bandgap. Thus, we expect one edge state propagating along the boundary of a mechanical lattice with uniform modulation $\{\phi_1,\phi_2,\phi_3\}=\{0,2\pi/3,4\pi/3\}$ or $\{4\pi/3,2\pi/3,0\}$. To confirm this behavior, we consider band structure and edge modes propagating on the external edges of a finite mechanical lattice with uniform modulation $\{\phi_1,\phi_2,\phi_3\}=\{0,2\pi/3,4\pi/3\}$, as well as edge modes that propagate along the boundary, as shown in Fig. 14. In the simulation, the supercell is composed of a 1×12 array of unit cells, terminated by a free boundary at the top and bottom and Floquet-Bloch boundary conditions along the *x*-direction. Figure 14(a) represents the band structure of the finite modulated lattice. Here, we focus on the frequency region of the four bulk bands of interest: the blue dots correspond to bulk modes, which form four bands separated by a gap. Different from Fig. 10, however, the truncated structure now supports two distinct modes within each bandgap. Inspection of the mode profiles, shown in Figs. 14(b) and (c), confirms that these bands correspond to modes localized on the top and bottom edges of the lattice, respectively. These modes have one-way characteristics with respectively positive (red dots) and negative (yellow dots) group velocities. It is interesting that the direction of edge states is dictated by the modulation handedness. Thus, it is can be deduced for the case $\{\phi_1,\phi_2,\phi_3\}=\{4\pi/3,2\pi/3,0\}$, that the top and bottom edge states correspond to positive and negative group velocities, respectively.

In a similar fashion, we calculate the interface states localized at the interface between two mechanical lattices with opposite modulation handedness; see Fig. 15. The sample is composed of 12 unit cells with periodic boundary conditions in both the *x*- and *y*-direction. The six top and bottom unit cells have opposite modulation handedness with $\{\phi_1, \phi_2, \phi_3\} = \{0, 2\pi/3, 4\pi/3\}$, and $\{4\pi/3, 2\pi/3, 0\}$, respectively. According to the principle of bulk-edge correspondence, the difference in the band Chern numbers between two half parts equals two, leading to a pair of interface modes in each bandgap region. Because of the periodic boundary conditions on the top and bottom boundaries of the supercell, another pair of interface modes are observed and therefore a total of four interface modes are expected within the bandgap region (shown by yellow and red dots in Fig. 15(a)), with two interface modes localized at every interface. It is noticed that two interface modes are again one-way in character: the yellow dots correspond to negative group velocities, while the red dots correspond to positive group velocities. Figures 15(b) and (c) confirm that the interface modes with negative group velocities are localized at the center of the supercell. However, the direction of propagation reverses at the bottom-top interfaces.

To realize topological one-way edge states absent of backscattering at corners, transient numerical simulations of a signal propagated along the boundary of a modulated mechanical lattice are conducted in a rectangular path. The constitutive and modulation parameters are $m = 1$, $k = 10$, $J = 0.5$, $v = 12$, and $\delta k = 0.3k$. We consider a sample containing 15×16 unit cells under free boundary conditions. The excitation is a narrow-band 200-cycle toneburst horizontal body force centered on $\omega = 3.93$ and applied at one mass as illustrated in Fig. 16. It shows two drastic examples of an elastic wave edge state that seamlessly propagates along the edges despite the presence of sharp corners in the hexagonal lattice. Figure 16(a) illustrates snapshots of waves

propagating clockwise for $\{\phi_1, \phi_2, \phi_3\} = \{0, 2\pi/3, 4\pi/3\}$, and Fig. 16(b) illustrates snapshots of waves propagating counterclockwise with the reversal of the modulation handedness. It is seen that the wave packet has no evidence of backscattering or bulk scattering due to its impact with the corners of the mechanical lattice. This scattering of the edge state is prevented by topological protection. However, in any natural elastic material, with topologically trivial properties, the corners would inherently couple forward and backward waves leading to reflections. On the contrary, the elastic edge states are immune to backscattering and exhibit strong protection against any kind of defect, providing robust and reconfigurable propagation over a broad bandwidth.

3.4 Robustness analysis

To support the abovementioned statement, we demonstrate this intriguing property using large-scale simulations of hexagonal lattices with a small defect implemented by removing nine masses at the top boundary, as seen in Fig. 17(a). It is observed that the topological edge modes with and without defects perform mostly the same by comparing the snapshots at different times in Figs. 16(a) and 17(a), which allow ideal reflection-less routing along the defined defects. In addition to topological robustness of the edge modes against structural defects, one-way transmission is protected by disorders in the modulation. To confirm the routing, we have generated a hexagonal lattice with random modulation of the phase in the trimers, as shown in Fig. 17(b). For disorder in phase delay, we allow ϕ_j, j = 1, 2, and 3 to be randomly displaced $\delta\phi_j$ with respect to its original phase delays $\{\phi_1, \phi_2, \phi_3\} = \{0, 2\pi/3, 4\pi/3\}$. It is seen that the 40% modulation disorder degree has no noticeable influence on the propagation of elastic edge waves. Thus, topological properties for in-plane elastic waves can be readily obtained in practice without requiring uniform phase of the modulation across lattices. Finally, topological immunity

to backscattering extends to the dissipation effect as well, as shown in Fig. 17(c), which is experimentally-unavoidable in the classical models. Note that the definition of is the same as the 1D protocol in Sec. 2.3. It is found that the chiral edge states in the topological mechanical systems are robust against the dissipation. To conclude that topological protection is absolute, the performance of the topological waveguide with three defects shown in Figs. 17(a), (b) and (c) is compared with the waveguide without defects. As shown in Fig. 17(d), it could be concluded that the response has little-to-no sensitivity to the presence of the defects for the interested frequency range. With these remarkable properties, our design constitutes a key step towards the practical implementation of robust, large-scale, Floquet topological insulators, even beyond this elastic implementation.

4. Conclusion

We have demonstrated numerically that time-modulated elastic lattices represent an ideal platform to implement a mechanical analogue of the QHE in 1D 3-periodic and 2D hexagonal lattices, taking a significant step towards practical and robust applications of topological elastic media. In 1D, relevant background on topological invariants due to time-modulated materials, how they arise in a classical mechanical context and how their existence influences the dynamic behavior within bandgaps, is provided in a simple framework. In 2D, we investigate the modulated hexagonal lattices switching from trivial to nontrivial topology by applying the proper time-modulation, leading to one-way transmission protected against backscattering by sharp corners, defects, modulation disorders, and dissipation effects. As an outcome, one-way topological elastic waves localized at the boundary of modulated lattices are fully characterized in terms of existence conditions, modal shapes, and immunity to scattering by various defects. Elastic topological insulators, in particular, hold the promise to revolutionize our ability to

control elastic waves, allowing for large isolation in the bulk and broadband one-way transport along their edges.

Acknowledgments

This work is supported by the Air Force Office of Scientific Research under Grant No. AF 9550-18-1-0342 with Program Manager Dr. Byung-Lip (Les) Lee, the NSF EFRI under award No. 1641078 and the Army Research office under Grant No. W911NF-18-1-0031 with Program Manager Dr. David M. Stepp.

REFERENCES

[1] S. Mittal, J. Fan, S. Faez, A. Migdall, J. M. Taylor, and M. Hafezi, Topologically robust transport of photons in a synthetic gauge field, Phys. Rev. Lett. **113**, 087403 (2014).

[2] R. Süsstrunk and S. D. Huber, Observation of phononic helical edge states in a mechanical topological insulator, Science **349**, 47 (2015).

[3] M. Z. Hasan and C. L. Kane, Colloquium: Topological insulators, Rev. Mod. Phys. **82**, 3045 (2010).

[4] X. L. Qi and S. C. Zhang, Topological insulators and superconductors, Rev. Mod. Phys. **83**, 1057 (2011).

[5] R. Fleury, D. L. Sounas, M. R. Haberman, and A. Alù, Nonreciprocal acoustics, Acoust. Today **11**, 14 (2015).

[6] S. A. Cummer, J. Christensen, and A. Alù, Controlling sound with acoustic metamaterials, Nat. Rev. Mater. **1**, 16001 (2016).

[7] K. L. Tsakmakidis, L. Shen, S. A. Schulz, X. Zheng, J. Upham, X. Deng, H. Altug, A. F. Vakakis, and R. W. Boyd, Breaking Lorentz reciprocity to overcome the time-bandwidth limit in physics and engineering, Science **356**, 1260 (2017).

[8] X. F. Li, X. Ni, L. Feng, M. H. Lu, C. He, and Y. F. Chen, Tunable unidirectional sound propagation through a sonic-crystal-based acoustic diode, Phys. Rev. Lett. **106**, 084301 (2011).

[9] N. Boechler, G. Theocharis, and C. Daraio, Bifurcation-based acoustic switching and rectification, Nat. Mater. **10**, 665 (2011).

[10] J. Maciejko, T. L. Hughes, and S. C. Zhang, The quantum spin Hall effect, Annu. Rev. Condens. Matter Phys. **2**, 31 (2011).

[11] J. Y. Lu, C. Y. Qiu, M. Z. Ke, and Z. Y. Liu, Valley vortex states in sonic crystals, Phys. Rev. Lett. **116**, 093901 (2016).

[12] J. Y. Lu, C. Y. Qiu, L. P. Ye, X. Y. Fan, M. Z. Ke, F. Zhang, and Z. Y. Liu, Observation of topological valley transport of sound in sonic crystals, Nat. Phys. **13**, 369 (2017).

[13] T. W. Liu and F. Semperlotti, Tunable acoustic valley-Hall edge states in reconfigurable phononic elastic waveguides, Phys. Rev. Appl. **9**, 014001(2018).

[14] R. K. Pal and M. Ruzzene, Edge waves in plates with resonators: an elastic analogue of the quantum valley Hall effect, New J. Phys. **19**, 025001 (2017).

[15] J. Vila, R. K. Pal, and M. Ruzzene, Observation of topological valley modes in an elastic hexagonal lattice, Phys. Rev. B **96**, 134307 (2017).

[16] X. Ni, M. A. Gorlach, A. Alù, and A. B. Khanikaev, Topological edge states in acoustic Kagome lattices, New J. Phys. **19**, 055002 (2017).

[17] H. Chen, H. Nassar, and G. L. Huang, A study of topological effects in 1D and 2D mechanical lattices, J. Mech. Phys. Solids **117**, 22 (2018).

[18] Y. Chen, X. N. Liu, and G. K. Hu, Topological phase transition in mechanical honeycomb lattice, J. Mech. Phys. Solids **122**, 54 (2019).

[19] H. Z. Lu, W. Yao, D. Xiao, and S. Q. Shen, Intervalley scattering and localization behaviors of spin-valley coupled Dirac fermions, Phys. Rev. Lett **110**, 016806 (2013).

[20] R. Fleury, D. L. Sounas, C. F. Sieck, M. R. Haberman, and A. Alù, Sound isolation and giant linear nonreciprocity in a compact acoustic circulator, Science **343**, 516 (2014).

[21] P. Wang, L. Lu, and K. Bertoldi, Topological phononic crystals with one-way elastic edge waves, Phys. Rev. Lett. **115**, 104302 (2015).

[22] L. M. Nash, D. Kleckner, A. Read, V. Vitelli, A. M. Turner, and W. T. M. Irvine, Topological mechanics of gyroscopic metamaterials, Proc. Natl. Acad. Sci. **112**, 14495 (2015).

[23] Z. J. Yang, F. Gao, X. H. Shi, X. Lin, Z. Gao, Y. D. Chong, and B. L. Zhang, Topological acoustics, Phys. Rev. Lett **114**, 114301 (2015).

[24] A. B. Khanikaev, R. Fleury, S. H. Mousavi, and A. Alù, Topologically robust sound propagation in an angular-momentum-biased graphene-like resonator lattice, Nat. Commun. **6**, 8260 (2015).

[25] R. Fleury, A. B. Khanikaev, and A. Alù, Floquet topological insulators for sound, Nat. Commun. **7**, 11744 (2016).

[26] H. Nassar, H. Chen, A. N. Norris, and G. L. Huang, Quantization of band tilting in modulated phononic crystals, Phys. Rev. B **97**, 014305 (2018).

[27] R. Chaunsali, F. Li, and J. K. Yang, Stress wave isolation by purely mechanical topological phononic crystals, Sci. Rep. **6**, 30662 (2016).

[28] G. Salerno, T. Ozawa, H. M. Price, and I. Carusotto, Floquet topological system based on frequency-modulated classical coupled harmonic oscillators, Phys. Rev. B **93**, 085105 (2016).

[29] F. Casadei, T. Delpero, A. Bergamini, P. Ermanni, and M. Ruzzene, Piezoelectric resonator arrays for tunable acoustic waveguides and metamaterials, J. Appl. Phys. **112**, 064902 (2012).

[30] Y. Y. Chen G. K. Hu, and G. L. Huang, An adaptive metamaterial beam with hybrid shunting circuits for extremely broadband control of flexural waves, Smart Mater. Struct. **25**, 105036 (2016).

[31] X. P. Li, Y. Y. Chen, G. K. Hu, and G. L. Huang, A self-adaptive metamaterial beam with digitally controlled resonators for subwavelength broadband flexural wave attenuation, Smart Mater. Struct. **27**, 045015, 2018.

[32] E. J. Redd, M. Soljačić, and J. D. Joannopoulos, Color of shock waves in photonic crystals, Phys. Rev. Lett. **91**, 133901 (2003).

[33] K. Danas, S. V. Kankanala, and N. Triantafyllidis, Experiments and modeling of iron-particle-filled magnetorheological elastomers, J. Mech. Phys. Solids **60**, 120 (2012).

[34] J. Gump, I. Finkler, H. Xia, R. Sooryakumar, W. J. Bresser, and P. Boolchand, Light-induced giant softening of network glasses observed near the mean-field rigidity transition, Phys. Rev. Lett. **92**, 245501 (2004).

[35] N. Swinteck, S. Matsuo, K. Runge, J. O. Vasseur, P. Lucas, and P. A. Deymier, Bulk elastic waves with unidirectional backscattering-immune topological states in a time-dependent superlattice, J. Appl. Phys. **118**, 063103 (2015).

[36] Y. F. Wang, B. Yousefzadeh, H. Chen, H. Nassar, G. L. Huang, and C. Daraio, Observation of nonreciprocal wave propagation in a dynamic phononic lattices, Phys. Rev. Lett. **121**, 194301 (2018).

[37] J. Vila, R. K. Pal, M. Ruzzene, and G. Trainiti, A Bloch-based procedure for dispersion analysis of lattices with periodic time-varying properties, J. Sound Vib. **406**, 363 (2017).

[38] D. J. Thouless, Quantization of particle transport, Phys. Rev. B **27**, 6083 (1983).

[39] Y. Hatsugai and T. Fukui, Bulk-edge correspondence in topological pumping, Phys. Rev. B **94**, 041102(R) (2016).

[40] T. Fukui, Y. Hastugai, and H. Suzuki, Chern numbers in discretized Brillouin zone: Efficient method of computing (spin) Hall conductances, J. Phys. Soc. Jpn. **74**, 1674 (2005).

[41] T. Mikami, S. Kitamura, K. Yasuda, N. Tsuji, T. Oka, and H. Aoki, Brillouin-Wigner theory for high-frequency expansion in periodically driven systems: Application to Floquet topological insulators, Phys. Rev. B **93**, 144307 (2016).

[42] A. Eckardt and E. Anisimovas, High-frequency approximation for periodically driven quantum systems from a Floquet-space perspective, New J. Phys. **17**, 093039 (2015).

Figures

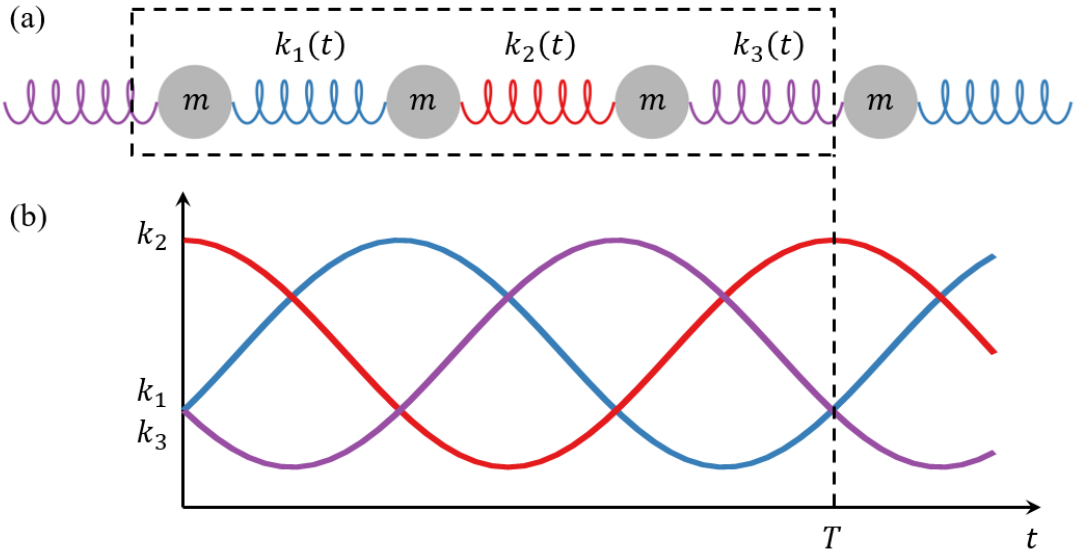

Fig. 1. A modulated 3-periodic spring-mass lattice: (a) Geometry; a unit cell is framed with dashed lines. (b) Time profiles of the modulated spring constants.

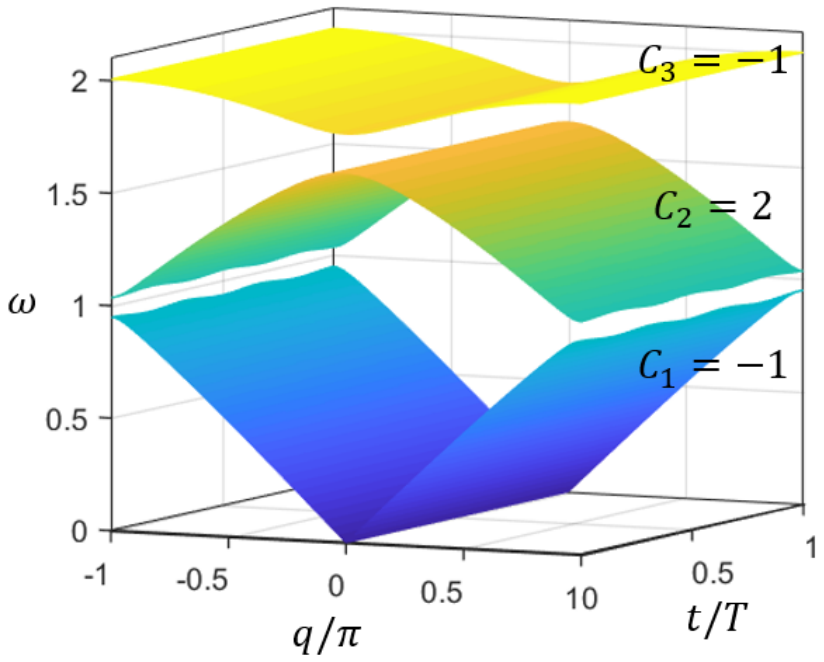

Fig. 2. Evolution of eigenfrequencies of an infinitely modulated lattice as a function of the non-dimensional wavenumber and time, with Chern numbers assigned to each band.

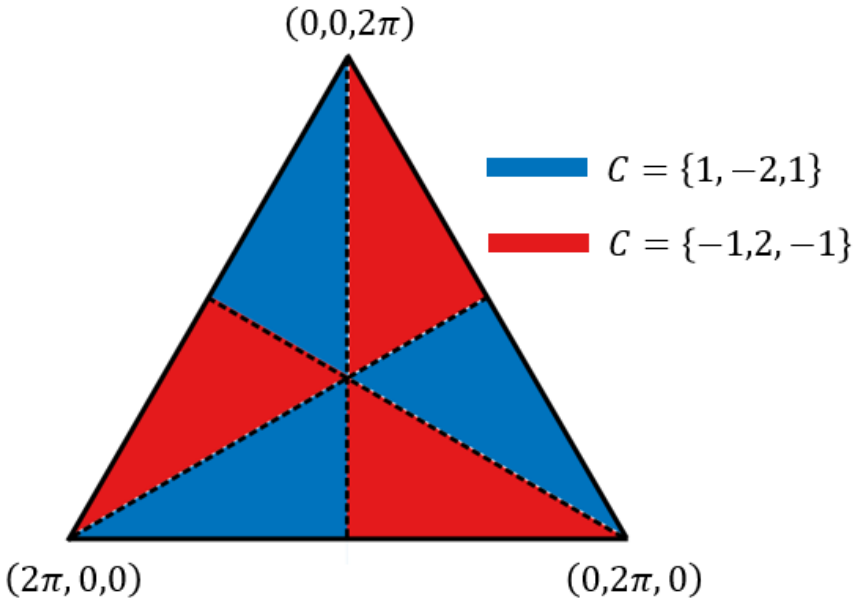

Fig. 3. Phase diagram of the 1D modulated lattice illustrating Chern numbers as a function of phase delays $\{\phi_1, \phi_2, \phi_3\}$ interpreted as barycentric coordinates in the planes ($\phi_1 + \phi_2 + \phi_3 = 2\pi$). Chern numbers are not defined over the dashed lines where degeneracies occur.

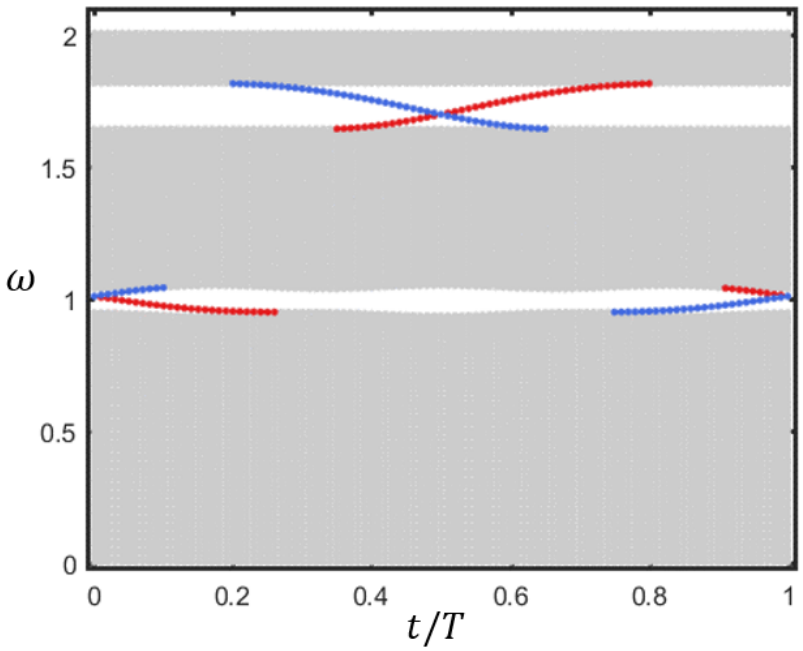

Fig. 4. Evolution of eigenfrequencies of a finite periodic lattice (300 masses) over one period of modulation under free boundary conditions. Two bandgaps are visible and are traversed by the eigenfrequencies of edge states. The shaded gray regions indicate the bulk pass bands. Left and right edge modes are highlighted by blue and red circles, respectively.

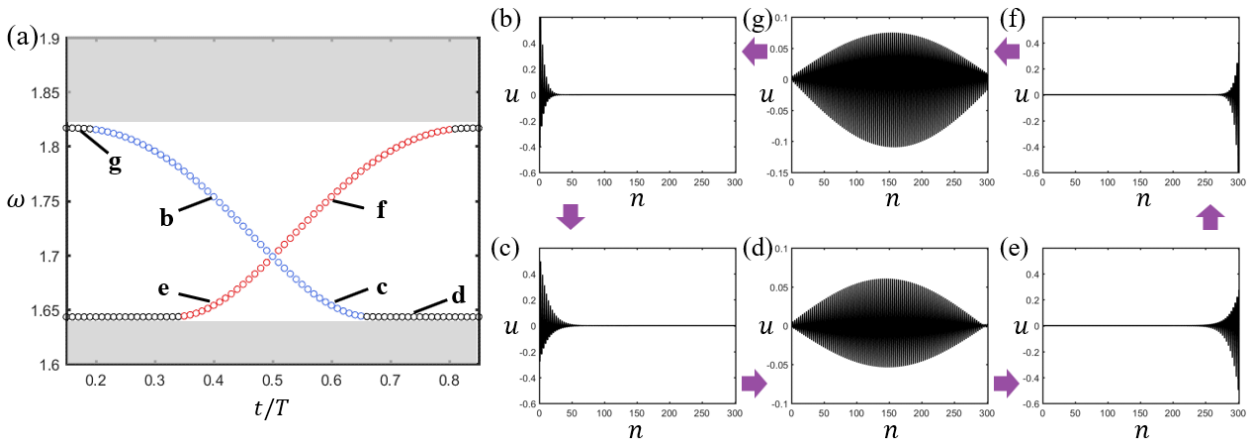

Fig. 5. (a) The edge states within the higher bandgap at $t = 0.4T$ and $t = 0.6T$ are labeled b, e, and c, f; the bulk states at $t = 0.75T$ and $t = 0.15T$ are labeled d and g. The corresponding eigenmodes as a function of position along the 1D lattice are plotted in (b)-(g), respectively, where n is the mass index and u the corresponding displacement amplitude. The shaded gray regions indicate the bulk pass bands.

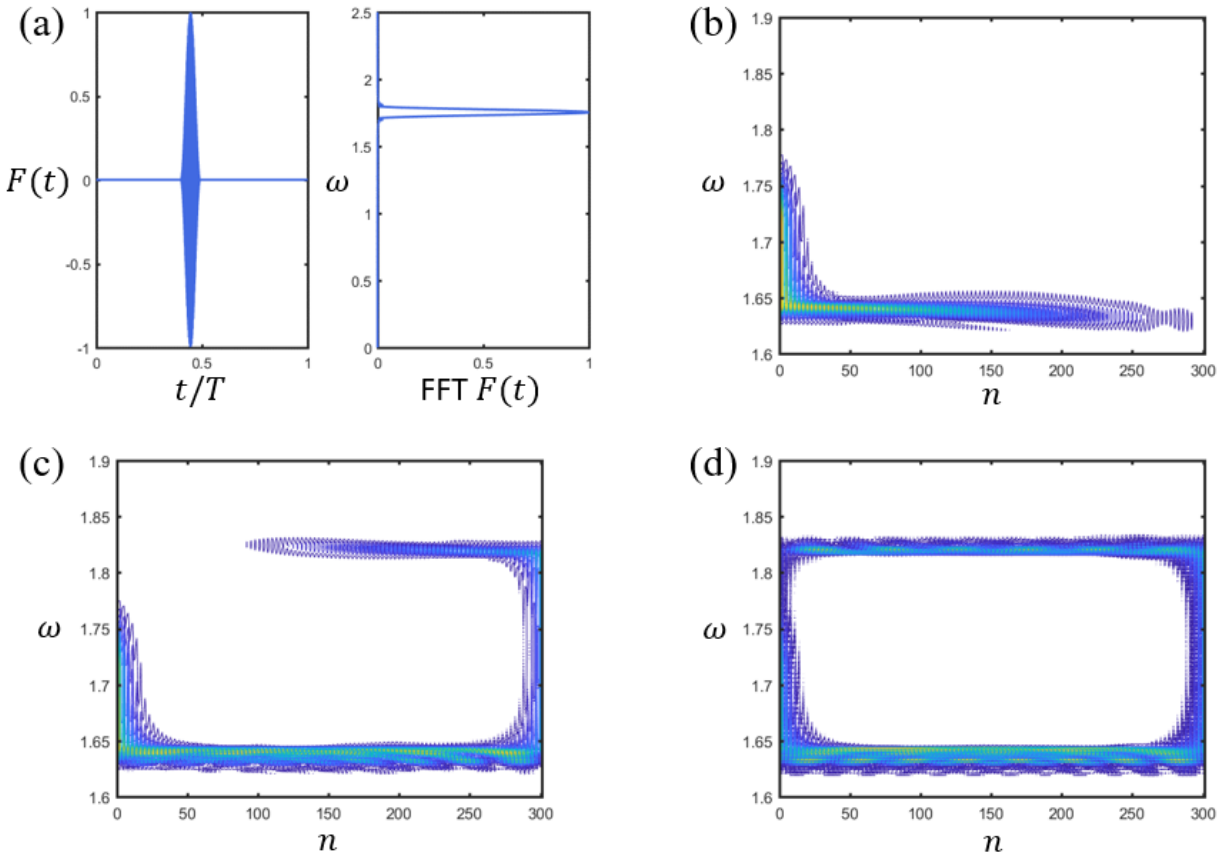

Fig. 6. (a) The transient force loading F in time and frequency domains; (b-d) The FFT of the wave field are taken at $t = T$, $2T$ and $3T$, respectively, illustrated as a one-way edge state in the (n, ω)-space.

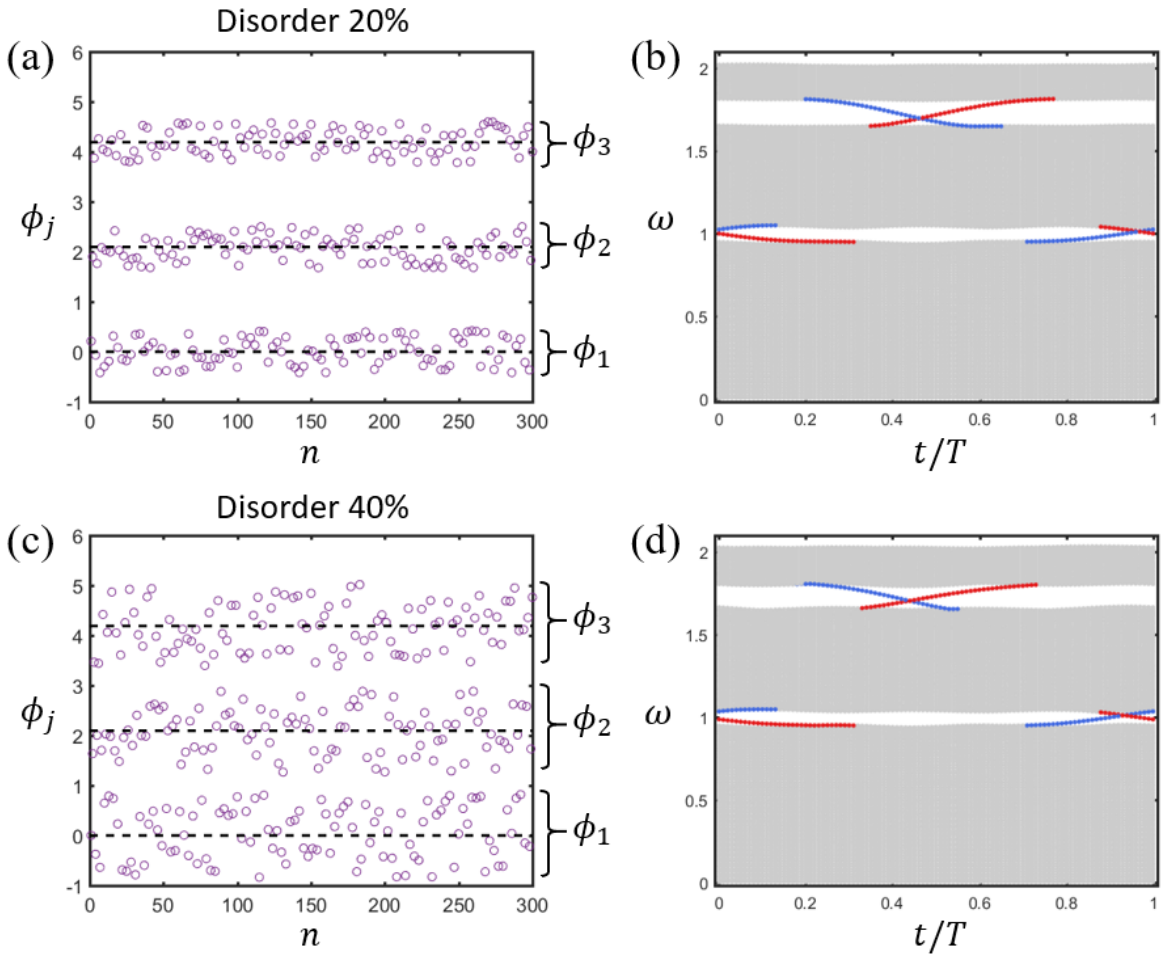

Fig. 7. Evolution of eigenfrequencies of a finite periodic lattice (300 masses) with random modulation phase disorders over one period of modulation under free boundary conditions. An example of phase disorder 20% (a) and the corresponding spectrum (b); an example of phase disorder 40% (c) and the corresponding spectrum (d); the purple circles in (a) and (c) show examples of the random profiles. The black dashed lines indicate original phase delays $\{\phi_1, \phi_2, \phi_3\} = \{0, 2\pi/3, 4\pi/3\}$. Left and right edge modes are highlighted by blue and red circles, respectively.

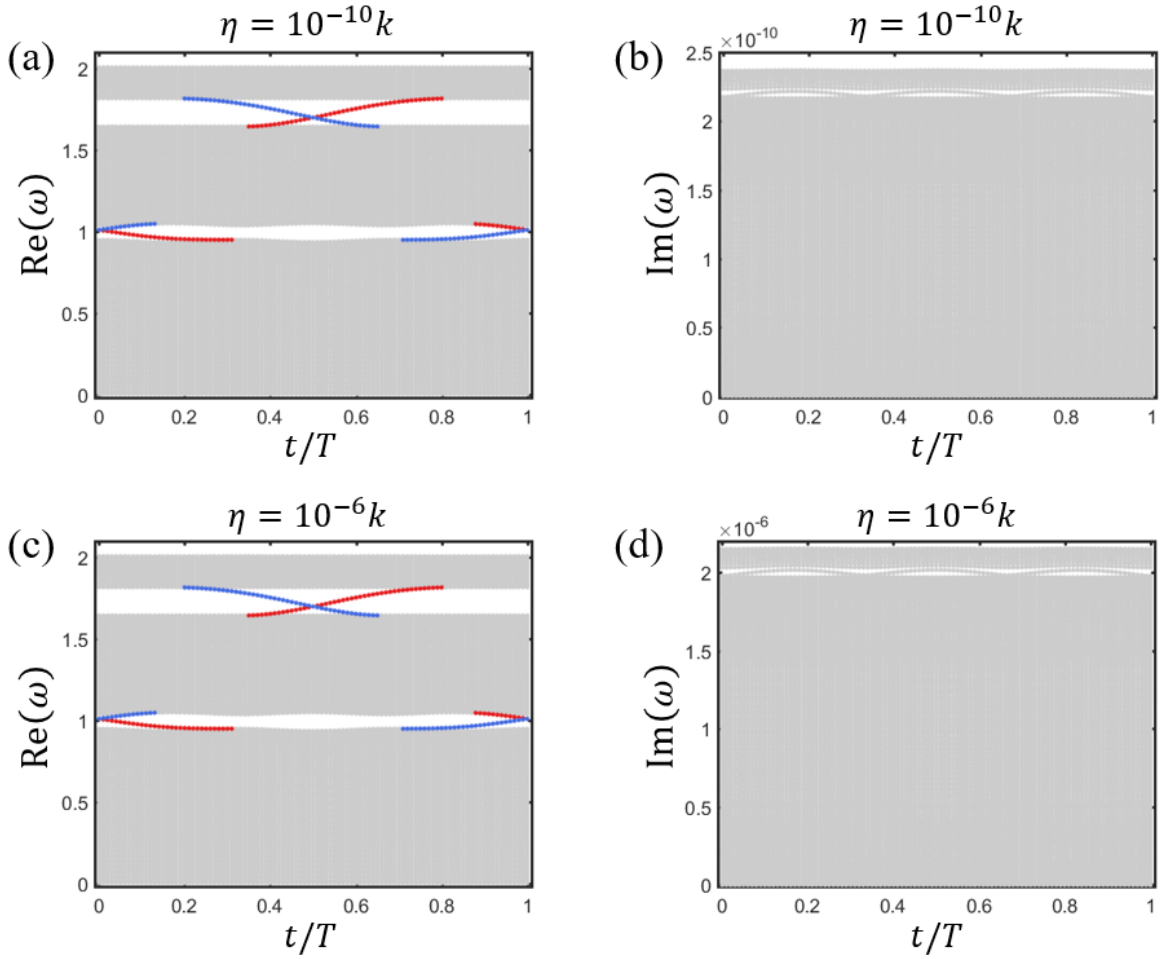

Fig. 8. Evolution of eigenfrequencies of a finite periodic lattice (300 masses) with different damping coefficients over one period of modulation under free boundary conditions. The real parts (a) and the imaginary parts (b) of the eigenfrequencies when $\eta = 10^{-10}k$; The real parts (c) and the imaginary parts (d) of the eigenfrequencies when $\eta = 10^{-6}k$. Left and right edge modes are highlighted by blue and red circles, respectively.

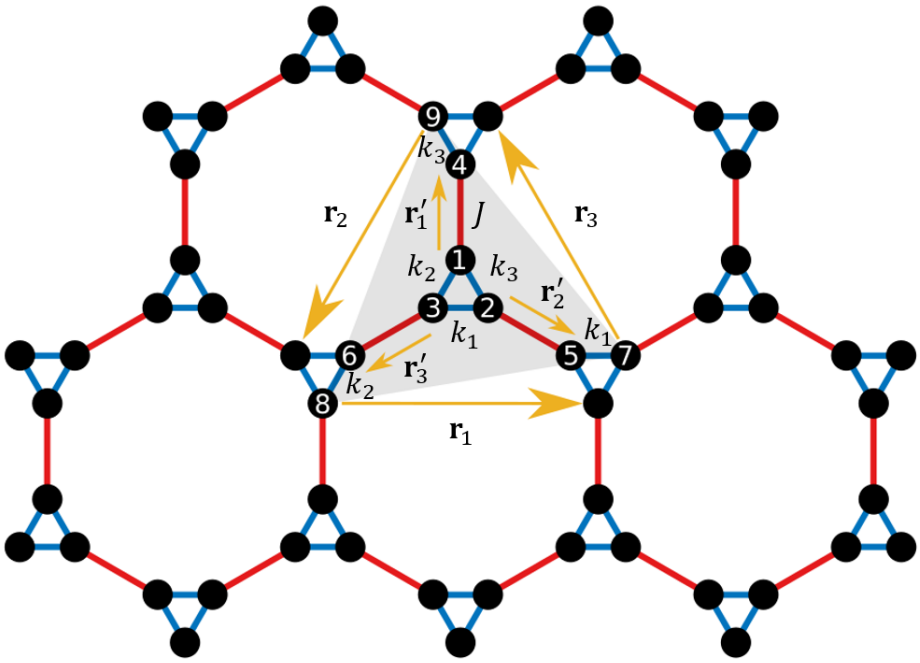

Fig. 9. A hexagonal lattice of modulated trimers composing of three interconnected masses, coupled with each other by modulated springs (blue edges). Edges are massless springs and black nodes are massive perfect hinges. The spring stiffness $k_j = k + \delta k \cos(\nu t + \phi_j)$ in trimers is periodically modulated in time at a frequency ν and with amplitude δk in a rotation fashion. The red edges show the nearest springs with constant J between modulated trimers. A unit cell is highlighted.

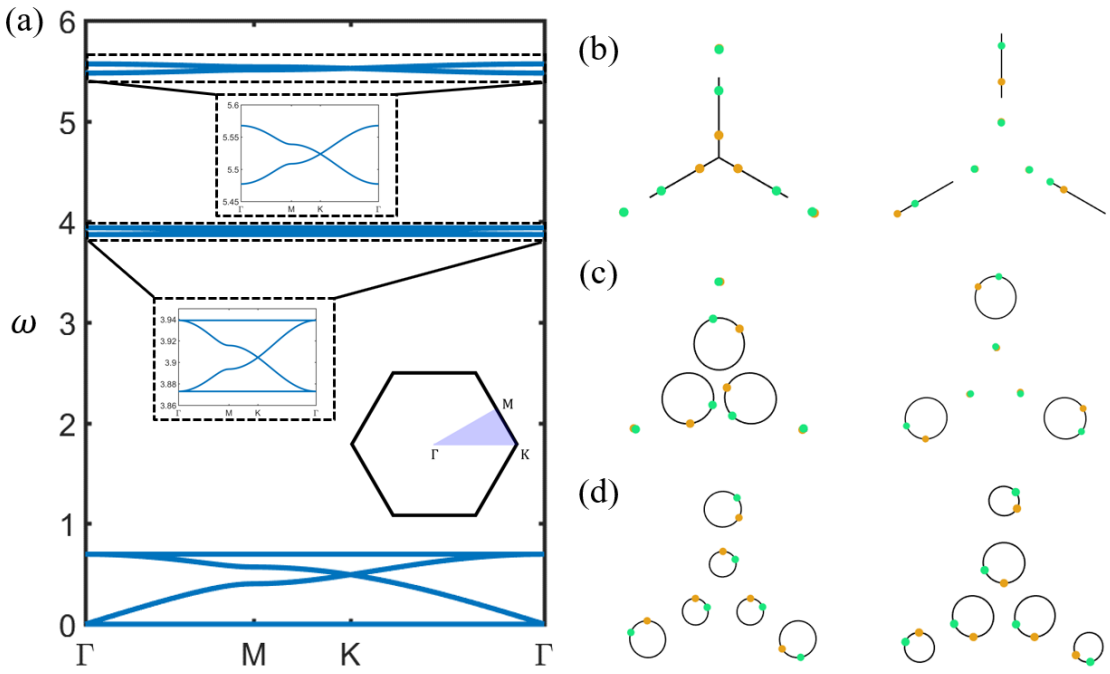

Fig. 10. (a) Dispersion diagrams for non-modulated hexagonal lattices (insets show zoomed view). As $\delta k = 0$, there are three degenerate points at K. The mass trajectories of the degenerate eigenstates are illustrated in (b) $\omega = 5.52$, (c) $\omega = 3.91$, and (d) $\omega = 0.49$, respectively. A yellow dot corresponds to the initial position of the mass and a green dot corresponds to the position at a later small time.

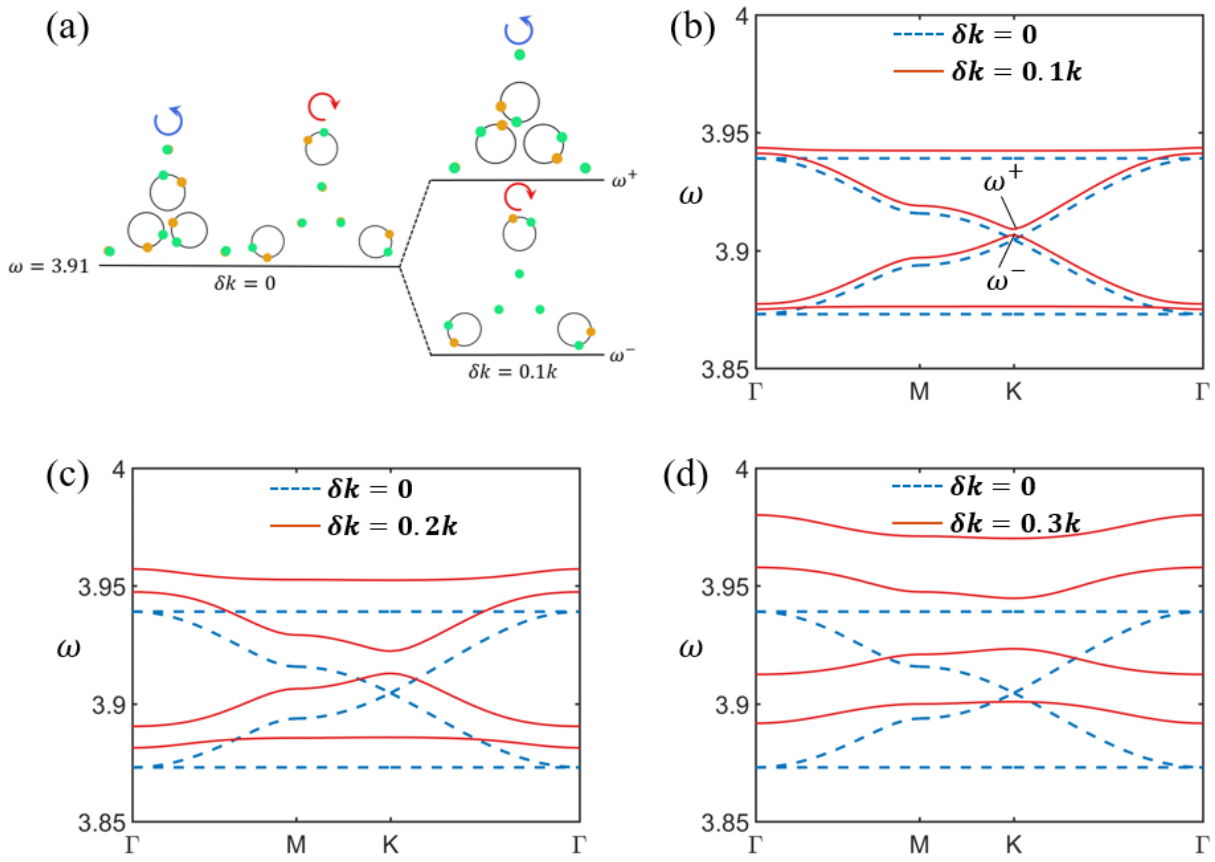

Fig. 11. (a) The modes split at ω = 3.91 due to angular momentum bias with modulation amplitude $\delta k = 0.1k$. The dispersion curves of non-modulated (blue dashed curves, $\delta k = 0$) and modulated hexagonal lattices (red solid curves, $\delta k = 0.1k$ in (b), $0.2k$ in (c), and $0.3k$ in (d)). Note that only four bands of interest are shown and the time modulation has the effect of folding the dispersion curves along the frequency axis.

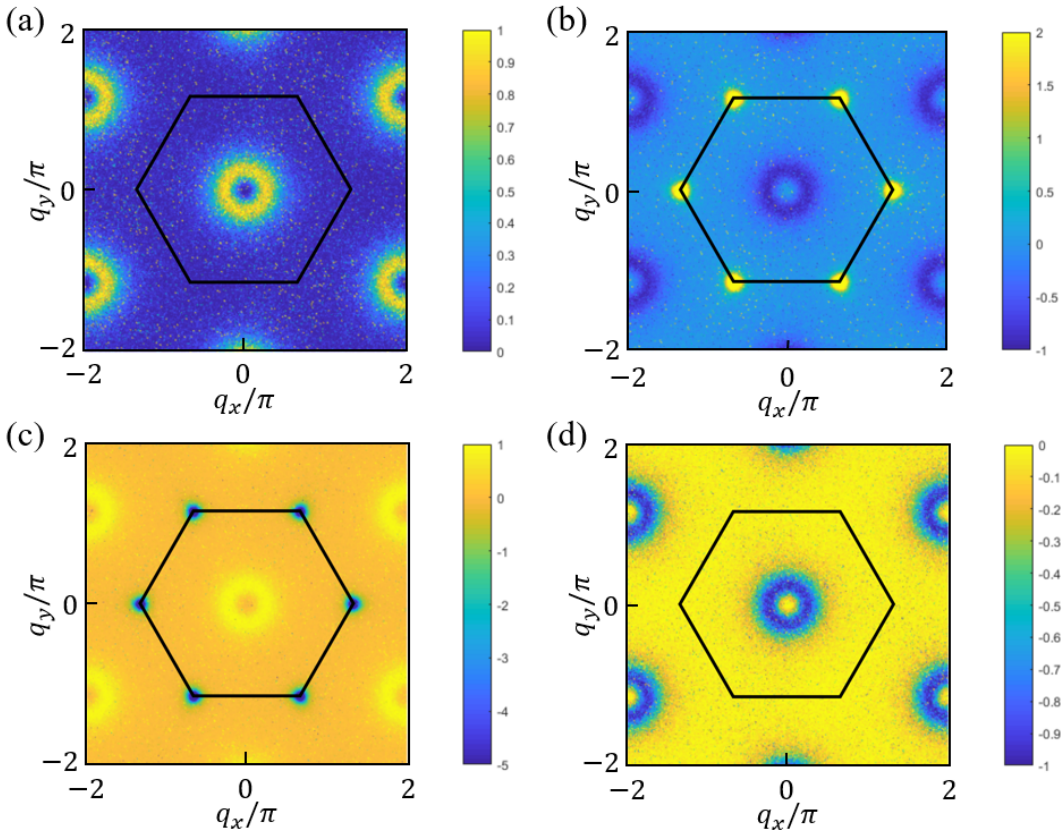

Fig. 12. Berry curvatures distribution in the Brillouin zone and its first Brillouin zone delimited by solid lines. (a)-(d) correspond to the four topological bands around the frequency of 3.91, from lower to higher frequency, respectively. The parameters used are $m = 1$, $k = 10$, $J = 0.5$, $\delta k = 0.1k$, $v = 12$, and $\{\phi_1, \phi_2, \phi_3\} = \{0, 2\pi/3, 4\pi/3\}$.

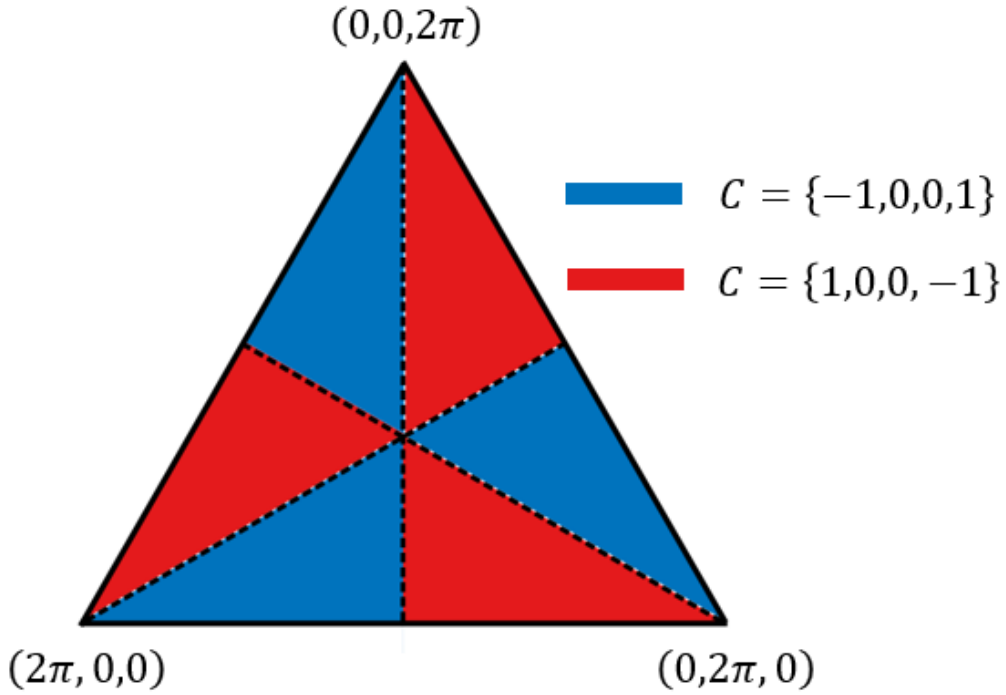

Fig. 13. Phase diagram of modulated hexagonal lattices illustrating Chern numbers as a function of phase delays $\{\phi_1, \phi_2, \phi_3\}$ interpreted as barycentric coordinates in the planes ($\phi_1 + \phi_2 + \phi_3 = 2\pi$). Note that the system is trivial over the dashed lines where phase transitions occur.

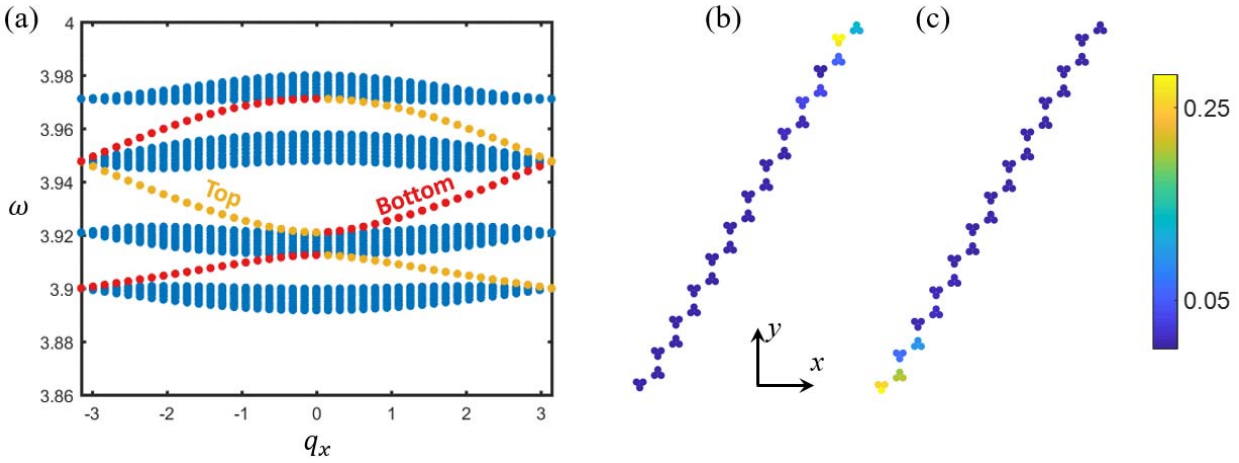

Fig. 14. (a) Bulk and edge spectra for a supercell of 12 unit cells under free boundary conditions at the top and bottom, and periodic boundary conditions in the x-direction. Bulk modes are shown by blue dots. Top (resp., bottom) edge modes are shown by yellow (resp., red) dots; (b)-(c) Mode profiles of the one-way edge mode localized at the top and bottom of the supercell, respectively, corresponding to the frequency $\omega = 3.93$.

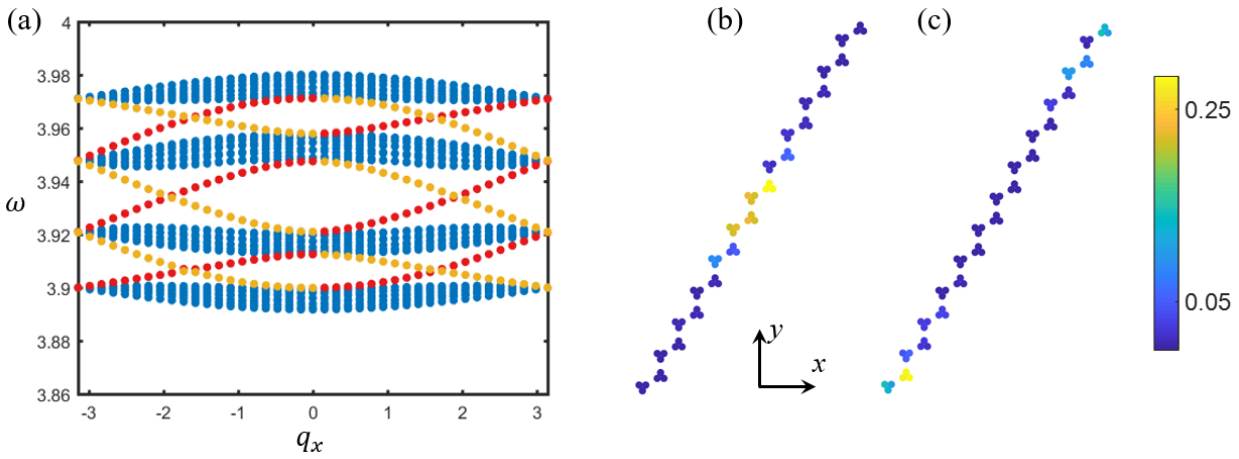

Fig. 15. (a) Bulk and edge spectra for a supercell of 12 unit cells supporting an interface at the center: the modulation of the 6 unit cells at the bottom $\{\phi_1, \phi_2, \phi_3\} = \{0, 2\pi/3, 4\pi/3\}$, and at the top $\{\phi_1, \phi_2, \phi_3\} = \{4\pi/3, 2\pi/3, 0\}$. Periodic boundary conditions are applied both in the x and y-direction. Bulk modes are shown by blue dots; (b) Modes associated with yellow dots are localized in the center of the supercell, while (c) red dots refer to interface modes are localized at the external edges of the supercell when ω = 3.93. Note that there are two interface modes in total in the center or at the external edges of the supercell but only one of them are shown for clarity.

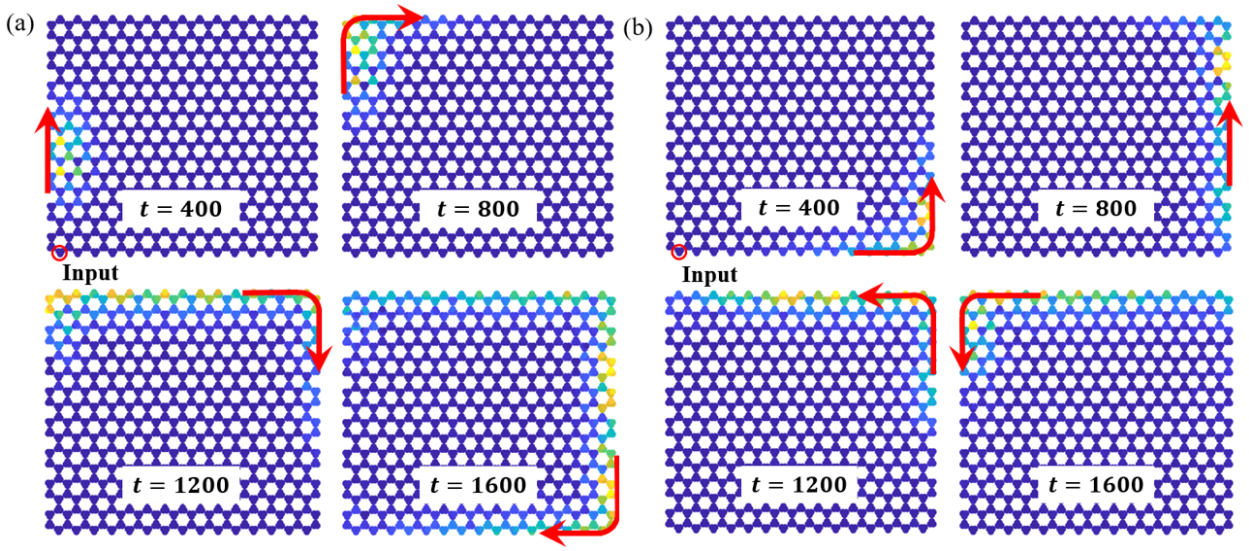

Fig. 16. Snapshots of one-way transmission of topological edge states with no backscattering at corners: (a) snapshots of the displacement amplitude as a color map for $\{\phi_1, \phi_2, \phi_3\} = \{0, 2\pi/3, 4\pi/3\}$, at t = 400, t = 800, t = 1200, and t = 1600, respectively; (b) snapshots of the displacement amplitude as a color map for $\{\phi_1, \phi_2, \phi_3\} = \{4\pi/3, 2\pi/3, 0\}$, at t = 400, t = 800, t = 1200, and t = 1600, respectively.

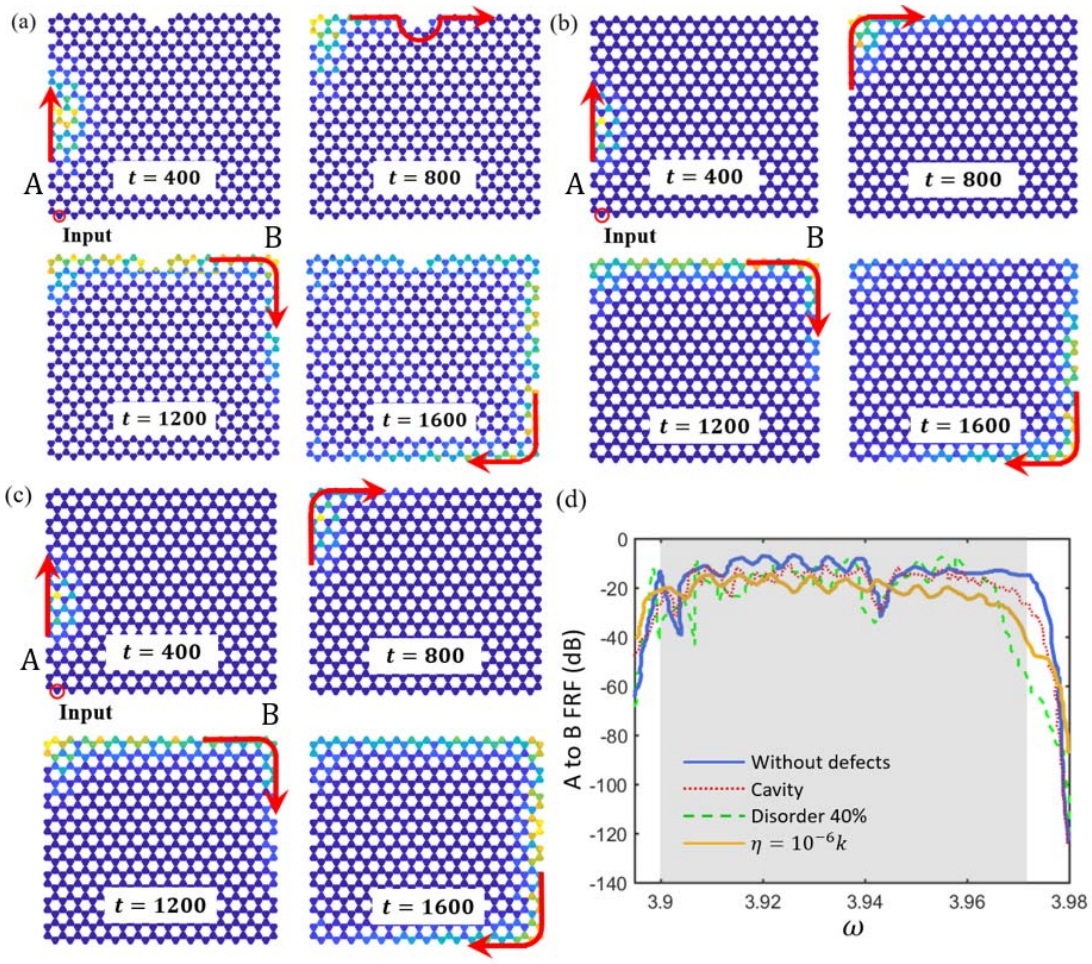

Fig. 17. Robustness demonstration of one-way transmission of topological edge states: (a) snapshots of the displacement amplitude with a cavity for $\{\phi_1, \phi_2, \phi_3\} = \{0, 2\pi/3, 4\pi/3\}$, at $t = 400$, $t = 800$, $t = 1200$, and (4) $t = 1600$, respectively; (b) snapshots of the displacement amplitude with 40% modulation disorders at $t = 400$, $t = 800$, $t = 1200$, and (4) $t = 1600$, respectively; (c) snapshots of the displacement amplitude with the damping coefficient $\eta = 10^{-6}k$, at $t = 400$, $t = 800$, $t = 1200$, and (4) $t = 1600$, respectively; (d) Frequency response functions for the one-way topological edge states with defects and without defects for the interested frequency range. The blue solid curve corresponds to the case without any defects, while the red dotted, green dashed and yellow solid curves correspond to the case with a cavity, random modulation disorders and dissipation effects, respectively.